Journal of Materials Processing Tech. 330 (2024) 118464

Contents lists available at ScienceDirect

Journal of Materials Processing Tech.

journal homepage: www.elsevier.com/locate/jmatprotec

Research article

# Influence of travel speed on microstructure and mechanical behavior of Inconel 625 fabricated using wire fed laser directed energy deposition

Jakub Preis [a,b], Stephanie B. Lawson [a,b], Isshu Lee [a], Megumi Kawasaki [a], Brian K. Bay [a], Sriram Manoharan [c], Brian K. Paul [a,b], Somayeh Pasebani [a,b,*]

[a] School of Mechanical, Industrial, and Manufacturing Engineering, Oregon State University, Corvallis, OR, 97330, United States of America
[b] Advanced Technology and Manufacturing Institute (ATAMI), Corvallis, OR, 97330, United States of America
[c] ADDiTEC, Palm City, FL, 34990, United States of America

ARTICLE INFO

*Keywords:*
Inconel 625
Microstructure
Mechanical properties
Superalloys
Wire laser directed energy deposition

ABSTRACT

The printing of Inconel 625 via wire-fed laser directed energy deposition is required for the near net shape fabrication of large scale components. In this study, an array of processing parameters was tested to identify a defect-free low-travel-speed and high-travel speed parameter for wire-fed laser directed energy deposition of Inconel 625. Samples printed using these parameters were subject to characterization in terms of grain morphology and tensile properties. Results showed that the high-travel-speed parameter had a refined columnar+equiaxed grain structure, whereas the low-travel-speed parameter had a columnar grain structure. The experimentally observed microstructure is correlated to the processing parameters by calculation of the solidification rate and thermal gradient. When tested perpendicular to the build direction, both parameters exhibited a similar yield strength. When tested parallel to the build direction, the high-travel-speed parameter exhibited a higher yield strength than the low-travel-speed parameter. For both parameters, samples pulled parallel to the build-direction showed a lower yield strength than samples pulled perpendicular to the build direction. The differences in yield strength for differing parameters and orientation are attributed primarily to dislocation strengthening.

## 1. Introduction

In recent years, the additive manufacturing (AM) method of wire laser directed energy deposition (wire-LDED) has been increasingly utilized over traditional manufacturing methods to fabricate high performance metal components. A comprehensive review of this AM process is provided by Ghanadi and Pasebani [1]. Compared with other AM methods, wire-LDED is characterized by high material utilization, a large print envelope, high print speed and the ability to fabricate near net shape parts. A popular material within the aerospace, chemical, and nuclear industries which can be printed using wire-LDED is Inconel 625. This alloy is noted for its high temperature strength coupled with excellent corrosion and fatigue resistance, making it the material of choice for applications such as rocket exhaust chambers as reported by Preis et al. [2,3].

A fundamental difficulty in net shape wire-LDED printing lies in the anisotropy that comes with wire feed direction. First approaches to wire-LDED systems consisted of an axial laser beam which creates the melt pool by melting a laterally fed wire as reported by Harwell et al. [4]. Syed et al. [5] showed that a better bead quality is achieved when the wire is fed to the front of the melt pool as compared to the back. Therefore, to achieve a consistent bead quality, multi-layer part printing is constrained to beads deposited in one direction (e.g. +x). This means that parts which require orthogonal placed beads (for example, in the +/− $y$ direction) are difficult to fabricate, severely hampering wire-LDED design freedom and print speed. In recent years, direction independent printing has been achieved by use of an axially fed wire which is melted by symmetrically placed lasers angled towards the wire, as reported by Nowotny et al. [6] and Kelbassa et al. [7]. Bambach et al. [8] used such a wire-LDED system equipped with a hexagonal laser setup to study the multi-layer printing of Inconel 718. The fabricated samples were free of process induced defects, indicating that axially-fed wire systems constitute a path forward for multi-layer wire-LDED printing.

Inconel 625 has been fabricated using the AM processes of laser powder bed fusion (LPBF), powder-LDED, and Wire Arc AM (WAAM), and the resultant microstructures and mechanical properties have been

* Corresponding author at: School of Mechanical, Industrial, and Manufacturing Engineering, Oregon State University, Corvallis, OR, 97330, United States of America.
*E-mail address:* somayeh.pasebani@oregonstate.edu (S. Pasebani).

https://doi.org/10.1016/j.jmatprotec.2024.118464
Received 1 March 2024; Received in revised form 22 May 2024; Accepted 3 June 2024
Available online 7 June 2024

**Table 1**
Composition of the Inconel 625 wire. C and S were analyzed using the combustion method. All other elements were determined by optical emission spectroscopy. All values in weight percent.

| Ni | Cr | Mo | Nb+Ta | Ti | Fe | Al | Si | V | Mn | C | P | Cu | Co | Others |
|---|---|---|---|---|---|---|---|---|---|---|---|---|---|---|
| 64.4 | 22.3 | 8.7 | 3.79 | 0.22 | 0.2 | 0.12 | 0.044 | 0.04 | 0.035 | 0.01 | 0.006 | 0.004 | 0.002 | 0.129 |

extensively studied. However, the fabrication of Inconel 625 using wire-LDED has been primarily investigated within the context of steel cladding, with relevant work published by Zhou et al. [9] and Abioye et al. [10]. This is mainly due to the lack of direction independence in wire-LDED systems with a latterly fed wire, as discussed previously. One exception lies in a study published by Gamon et al. [11], where a defect free wire-LDED Inconel 625 sample was printed and characterized in terms of grain size and microhardness as part of a comparison with other AM processes. However, no detailed microstructure characterization or mechanical property testing was conducted, and the study was not focused specifically on the wire-LDED process. Recently, Su et al. [12] fabricated Inconel 625 using wire-LDED to compare samples produced without wire preheating (cold wire-LDED) and with resistive wire preheating (hot wire-LDED). The researchers [12] reported a refined grain structure along with higher yield strength and elongation in samples printed using hot wire-LDED. However, the effect of processing parameters such as travel speed and laser power on the wire-LDED Inconel 625 was not studied. In addition, the authors used a wire-LDED system with an axial laser and laterally fed wire, therefore hampering the ability of the system to deposit material in all directions.

AM processing parameters have been shown to have an effect on the solidification rate ($R$) and thermal gradient ($G$) at the solidification front. Since the solidification rate and thermal gradient have been shown to govern the solidified microstructure, control of microstructure and corresponding mechanical proprieties of AM parts can be exercised by selectively altering processing parameters. A comprehensive review of the relationship between microstructure and both the solidification rate and thermal gradient is provided by Kou [13]. Raghavan et al. [14] developed a heat source model which was used to correlate processing parameters to the solidification rate and thermal gradient for electron beam AM Inconel 718. The researchers [14] reported that a greater beam-spot-on time and beam current results in a decreased thermal gradient, leading to a greater amount of equiaxed grains. Li et al. [15] fabricated Inconel 625 using WAAM, and reported a higher current parameter results in a lower thermal gradient, leading to a greater quantity of equiaxed grains. The sample fabricated using the higher current was shown to exhibit a 36% increase in yield strength. However, the influence of processing parameters on the solidification rate and thermal gradient for the wire-LDED process remains a gap within the prevailing literature.

This work addresses the prevailing research gap by utilizing a axially fed wire, six-laser wire-LDED system investigate the influence of processing parameters on microstructure and mechanical properties of Inconel 625. To do this, a defect-free parameter space for both single-tracks and multi-layer samples is first outlined. The impact of process parameters on microstructure is then investigated in terms of morphology and grain size. Corresponding mechanical properties are measured as a function of processing parameters and direction of load application relative to the build direction. This study links process-structure–property relationships for Inconel 625 components fabricated using wire-LDED.

## 2. Experimental methodology

### 2.1. Materials and LDED process

Inconel 625 wire feedstock with 0.889 mm diameter was provided by Arcos Industries. The elemental composition of the Inconel 625 wire used for this study is provided in Table 1.

**Table 2**
Parameters used for single-track wire-LDED of Inconel 625.

| Parameter | Values |
|---|---|
| Laser power [W] | 200, 400, 500, 600, 700, 800, 1000, 1200 |
| Travel speed [mm/min] | 200, 400, 600, 800, 1000, 1200 |
| Wire extrusion ratio [–] | 1–1.3 |

A Meltio M450 wire-LDED machine was used for all sample fabrication. This system is equipped with six lasers which are angled at 25° relative to the $Z$-axis and placed symmetrically around an axially-fed wire. Each laser has a max power of 200 W (system max power is 1200 W), and emits a wavelength of 970–980 nm. Due to the angle of the lasers, distance from the wire nozzle tip to the deposition location (the working distance) corresponds to the overlap of the lasers with each other and with the wire. In this study, a working distance of 6 mm was used. This results in a spot size of approximately 2 mm. A schematic of the Meltio M450 system along with the laser-wire alignment at the 6 mm working distance is provided in Fig. 1a. Nitrogen was used as shielding gas with a flow rate of 10 L/min. A Meltio print head such as the one used for this study can be mounted onto subtractive CNC machines for dimensional accuracy and robots for large scale printing as shown in Fig. 1b and c, respectively.

Table 2 outlines the printing parameters tested for single-track deposition of wire-LDED Inconel 625. All samples were printed onto a 304 SS substrate of dimension 105 × 120 × 30 mm. Investigated laser powers range from 200 W to 1200 W, with increments of 100 W except for extremities where 200 W increments were tested. Travel speeds ranging from 200 mm/min to 1200 mm/min were tested at increments of 200 mm/min. The chosen increments and ranges of tested parameters allowed for the parameter space to be thoroughly explored. The wire extrusion speed to travel speed ratio varied from 1–1.3 as necessary to achieve stable deposition (e.g. continuous bead). Defect free single-track parameters were then used to fabricate multi-layer samples for further microstructure and mechanical properties investigation. The multi-layer samples used a hatch pattern rotation of 90° as shown in Fig. 1d and were fabricated to dimensions of 20 × 20 × 10 mm. A dwell time of <10 s occurred between each layer as the build plate was lowered for subsequent layer deposition. A bead-width to hatching-distance ratio of 0.7 was used based on previous research by Akbari et al. [16].

### 2.2. Microstructure characterization

Density was measured by Archimedes method according to ASTM B311-17 [17]. For microstructural characterization, samples were cut to dimensions of 10 × 10 × 5 mm from fabricated samples using wire electronic discharge machining (EDM) to expose the surface both parallel and perpendicular to the build direction (BD). They were then mounted and ground using SiC papers from 180 to 1200 grit. The samples were polished using a 1 μm alumina slurry, a 0.05 μm alumina solution, and a 0.05 μm silica solution. Lastly, the samples were subject to vibratory polishing for 12 h in a 0.02 μm silica solution. A similar polishing procedure has been previously shown to provide optimal electron backscatter diffraction (EBSD) micrograph quality by Wynick and Boehlert [18]. To reveal the microstructure, the samples were electroetched with Kalling solution (5 g of CuCl2, 100 mL of Hydrochloric acid and 100 mL of Ethanol) etchant using 10 V for 3 s. The microstructure morphology was investigated using a Zeiss Axiotron optical microscope.

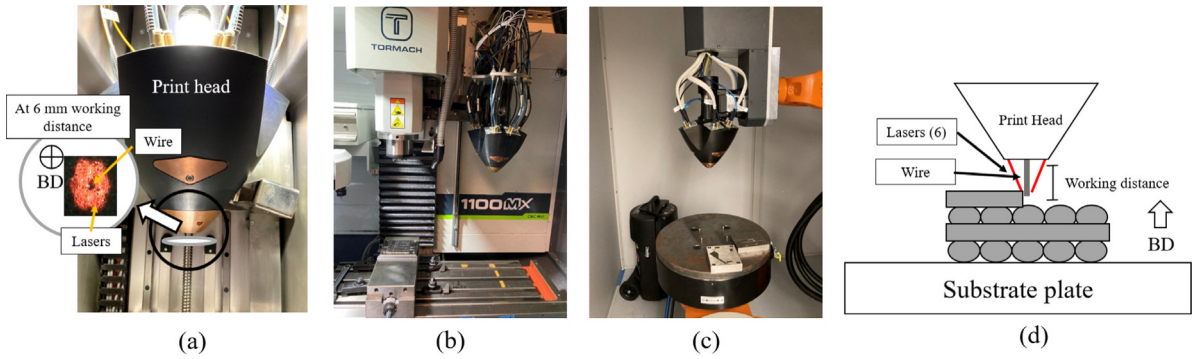


**Fig. 1.** (a) Picture of Meltio M450 print head with laser configuration at a working distance of 6 mm and (b) picture of Meltio print head mounted on a Tormach CNC, (c) picture of Meltio print head mounted on a Kuka robot, (d) schematic of printing showing a 90° hatch rotation every layer.

Two sets of EBSD scans were conducted: (1) a low-magnification scan with a step size of 1.1 μm for investigation of grain morphology, and (2) a high-magnification scan with a step size of 0.5 μm for calculation of dislocation density using kernel average misorientation (KAM). An FEI Quanta 3D dual beam scanning electron microscope (SEM) was used for both scans. For the low-magnification scans, the EBSD micrographs were cleaned using grain dilation in AMETEK OIM software with a minimum grain size of 1 and a grain tolerance angle of 5 (these are dimensionless parameters in the software). For the high-magnification scan, all points with a confidence index less than 0.03 (this is a dimensionless parameter in the software) were not considered because they are assumed to be erroneous solutions. This was done to filter out noise from the KAM measurements.

### 2.3. Calculation of solidification rate and thermal gradient

To understand how processing parameters effect solidification conditions, the solidification rate $R$ and thermal gradient $G$ were calculated. The $R$ for a given melt pool was found using Eq. (1) [19]:

$$R = \frac{V D}{L} \tag{1}$$

where $V$ is the travel speed, $D$ is the melt pool depth (orthogonal distance from the surface of the melt pool to the deepest point), and $L$ is the melt pool length (distance from the center of the melt pool to the trailing edge). To find melt pool depth $D$ and melt pool length $L$ for a parameter of interest, a wire-LDED coupled thermo-fluid model was used. Further details of this model are provided in section 2.2 of Lawson et al. [20]. The thermal gradient $G$ was then found based off the cooling rate $C_l$ using Eq. (2).

$$G = \frac{C_l}{R} \tag{2}$$

To find $C_l$, a type C thermocouple was placed under a Inconel 625 wire-LDED single track given a parameter of interest. The $C_l$ was calculated as the slope of the temperature–time curve at liquidus temperature to capture the cooling rate during solidification.

### 2.4. Mechanical testing

Micro-tensile samples were cut using wire EDM to test mechanical properties as shown in Fig. 2 (gauge dimensions: thickness 1.5 mm, length 5.7 mm, width 2 mm). Micro-tensile samples have been increasingly used to test the strength of AM components while limiting required print size [21]. The micro-tensile bar used in this study is specifically designed so that the gauge width and thickness are large enough to encompass multiple voxel elements (i.e. dimensions of single-track deposition), ensuring that inter-bead microstructure and defects are reflected in the tensile results. A preliminary study comparing mechanical properties as tested by standard ASTM E8 sample

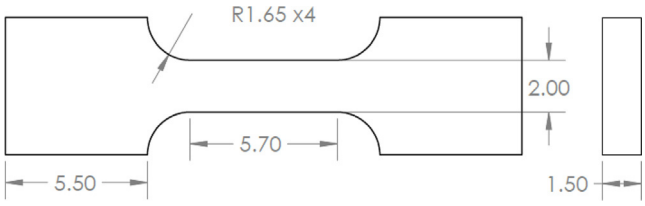


**Fig. 2.** Schematic showing dimensions of micro-tensile bar. All dimensions are in mm.

**Table 3**
Itemized DIC setup.

| | |
|---|---|
| Camera | FLIR blackfly S |
| Image size | 5472 px × 3548 px |
| Lens | Kowa LM25FC24M |
| Focal length | 25 mm |
| Aperture | f/15 |
| Field-of-view | 57.6 mm × 37.3 mm |
| Image Scale | 95 px/mm |
| Image acquisition rate | 1 Hz |

geometry and the micro-tensile geometry is provided in Appendix A. The samples were cut both parallel and perpendicular to the BD. A minimum of three tensile samples were tested for each processing condition and orientation relative to the BD.

The micro-tensile samples were tested on a Testing Resources 140 series frame at a strain rate of $2 \times 10^{-3}$ $s^{-1}$. Images of the tensile samples were collected using a pair of cameras to allow for 3D strain measurement using digital image correlation (DIC). Prior to testing, the gauge length of the tensile samples was coated in white paint after which a black speckle pattern was applied using spray paint. DIC camera specifics are provided in Table 3. LED light sources with polarization filters installed were mounted next to the cameras to reduce reflection through cross-polarization. The DIC setup was assembled based on DIC best practices outlined by Jones et al. [22]. Strain was extracted from the images using Vic-3D software, with a subset of 39 px, step of 3 px, and filter size of 7 data points. The strain data was matched to the load cell data by timestamp to generate stress–strain curves.

### 2.5. Calculating grain boundary strengthening and dislocation strengthening

To correlate microstructure to mechanical properties, grain boundary strengthening and dislocation strengthening were calculated.

#### 2.5.1. Grain boundary strengthening

A difference in yield strength due to grain boundary strengthening was modeled using the empirical Hall-Petch relationship, provided

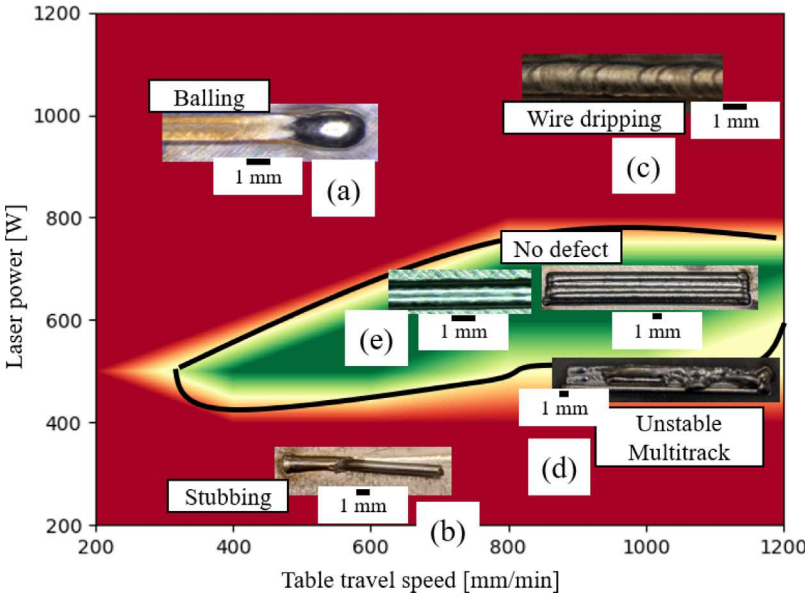


**Fig. 3.** Single-track and multi-track defect map (red shows defective parameter space, green shows defect-free parameter space) showing (a) balling, (b) stubbing, (c) wire dripping, (d) unstable multi-track, and (e) defect free regions. (For interpretation of the references to color in this figure legend, the reader is referred to the web version of this article.)

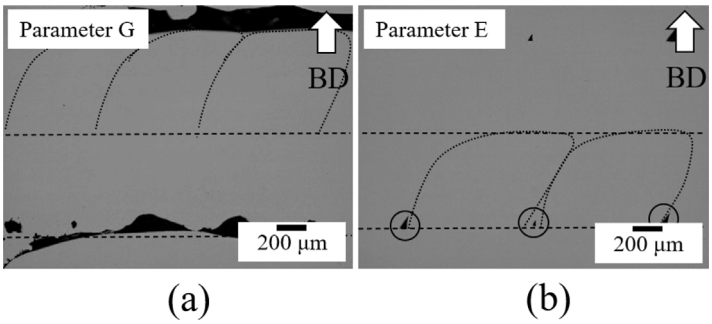


**Fig. 4.** Optical micrographs showing (a) lack of inter-layer adhesion in Parameter G (700 W, 1200 mm/min) and (b) pores at the roots of the bead in Parameter E (600 W, 1000 mm/min).

in Eq. (3) [23]:

$$\Delta\sigma_{GB} = \Delta k d^{-0.5} \tag{3}$$

where $\Delta\sigma_{GB}$ is the change in yield strength due to grain size effects, and $k$ is a constant called the Hall-Petch coefficient (which has been reported as 750 MPa $\mu m^{1/2}$ for Ni-based superalloys such as Inconel 625 [24]). $d$ is the average grain diameter, and was calculated from the low-magnification EBSD scans.

#### 2.5.2. Dislocation strengthening

The difference in yield strength due to dislocation strengthening was modeled using the Taylor relationship, provided in Eq. (4) [15]:

$$\Delta\sigma_D = \Delta M \alpha G b \sqrt{\rho} \tag{4}$$

where $M$ is the Taylor factor, $\alpha$ is a constant, $G$ is the shear modulus (72 GPa for Inconel 625 [25]), $b$ is the burgers vector (0.267 nm for Inconel 625 [25]), and $\rho$ is the dislocation density. The Taylor factor $M$ captures the influence of crystallographic texture on yield strength given a macroscopic stress state [26], and was calculated based on the low-magnification EBSD micrographs using the AMETEK OIM software. The $\alpha$ constant captures the effect of the dislocation pattern on dislocation slip, and in this study was set equal to 0.15 [27].

The dislocation density $\rho$ was calculated by considering geometrically necessary dislocations (GND) derived from KAM as shown in Eq. (5) [28].

$$\rho = \frac{2\theta}{ub} \tag{5}$$

where $\theta$ is the misorientation angle (KAM) between given points, $u$ is the unit length, and $b$ is the burgers vector. The unit length $u$ is the product of the step size used in the EBSD scan and the nearest neighbor choice (i.e. second nearest neighbor means that the misorientation is calculated based on points two points away from the target point), both of which can alter the $\rho$ calculation. To eliminate this ambiguity, Kamaya [29] showed that the $\frac{\theta}{u}$ term in Eq. (5) can be replaced by the slope $\frac{d\theta}{du}$. In this study, the average KAM was calculated for the first 5 nearest neighbors based off the high-magnification EBSD micrograph (as will be shown in Fig. 7a-d). The linear trendline slope was used for the $\frac{\theta}{u}$ value, thus allowing for the calculation of the dislocation density $\rho$ to plug into Eq. (4) for calculation of dislocation strengthening.

## 3. Results and discussion

### 3.1. Defect-free wire-LDED parameter space

Single-track and multi-track defects as a function of travel speed and laser power are shown in Fig. 3a-e. Defect-free parameter combinations are shown in green, while defect-inducing parameter combinations are shown in red. Defects are categorized as balling, stubbing, wire

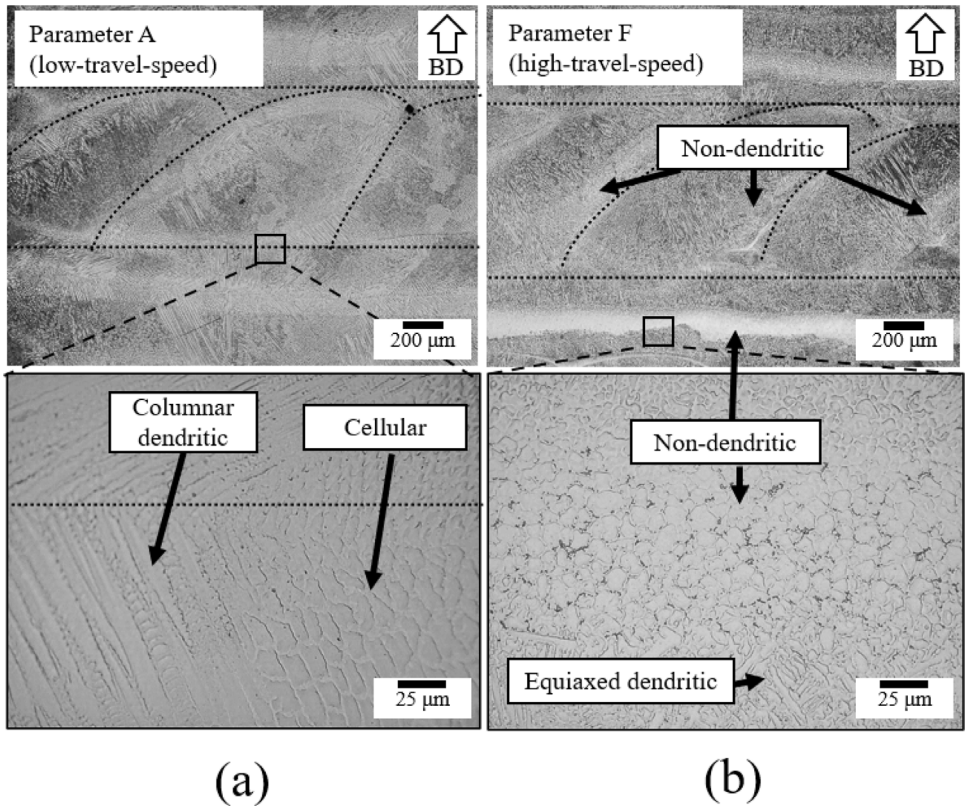


**Fig. 5.** Optical micrographs of the (a) Parameter A (low-travel-speed), (b) Parameter F (high-travel-speed) sample. A columnar dendritic structure is observed in (a) while non-dendritic regions along with equiaxed dendritic regions are observed in (b).

dripping, and unstable multitrack. Balling (Fig. 3a) occurs at low speeds and high laser powers, and results from the lasers melting the wire prior to creating a melt pool. Stubbing (Fig. 3b) occurs due to low laser power, leading to insufficient energy to melt the wire. Wire dripping (Fig. 3c) occurs at high speeds and high laser power. Research by Akbari et al. [16] and Bozeman et al. [30] shows that this is caused by premature wire melting. High-travel-speeds result in unstable multi-tracks due to the wire being pulled out of the melt pool as the table direction is changed (Fig. 3d). While a large area within the parameter space was found to contain defects, defect-free parameters (Fig. 3e) were identified in laser powers ranging from 500–700 W and travel speeds of 400–1200 mm/min. The parameter space was outlined in a way that clearly outlines the defect-free combinations for wire-LDED of Inconel 625.

Defect-free parameters shown in Table 4 were used to print multi-layer samples for density measurement and microstructure characterization. All samples have a relative density of >0.998 as measured by Archimedes method [31] except for the sample printed using parameter G. The relatively lower density of the parameter G sample is attributed to the lack of adhesion which occurred between layers due to high-travel-speed. This resulted in unstable deposition as shown in Fig. 4a. In a majority of the samples, pores were observed at the bead roots as shown in Fig. 4b.

### 3.2. Grain morphology, grain size, and KAM

The microstructure of parameters A, B, C, and D is characterized by a columnar dendritic morphology as shown in Fig. 5a. A similar morphology was observed in powder-LDED Inconel 625 by Rombouts et al. [32], and indicates that the wire-LDED fabricated samples experience a similar thermal history as powder-LDED. In higher travel speed parameters E, F, and G an equiaxed dendritic morphology is observed towards the top and bottom of each bead and non-dendritic regions are observed towards the middle of each bead as shown in Fig. 5b.

**Table 4**
Wire-LDED process parameters of multi-layer Inconel 625.

| Parameter | Laser power W | Travel speed mm/min | Hatch spacing mm |
|---|---|---|---|
| A[a] | 500 | 400 | 0.96 |
| B | 500 | 600 | 0.93 |
| C | 600 | 600 | 1.05 |
| D | 600 | 800 | 1.01 |
| E | 600 | 1000 | 0.96 |
| F[a] | 700 | 1000 | 0.94 |
| G | 700 | 1200 | 0.83 |

[a] Throughout this paper, wire-LDED process parameter A is used subsequently for characterization as the low-travel-speed parameter, while Parameter F is used as the high-travel-speed parameter.

For subsequent investigation, Parameter A was selected as representative of a slow-travel-speed parameter, while Parameter F was selected as representative of a high-travel-speed parameter. To characterize grain structure, low-magnification EBSD was performed on low-travel-speed and high-travel-speed samples as shown in Fig. 6a-d. The grain size distribution for each EBSD micrograph is provided in Appendix B. The low-travel-speed sample consists of epitaxial columnar grains elongated in the BD as shown in Fig. 6a. The grains were notably smaller when viewed perpendicular to the BD (Fig. 6b). In the high-travel-speed sample, a bimodal grain size distribution was observed with columnar+equiaxed grains towards the top and bottom of each bead and randomly textured ultra-fine grains towards the middle of the bead (Fig. 6c and d). The columnar+equiaxed grains in the high-travel-speed sample (Fig. 6c) towards the top and bottom of the bead have a visibly smaller diameter than the grains observed in the low-travel-speed sample (Fig. 6a).

The randomly textured ultra-fine grains in the high-travel-speed sample EBSD crystal orientation maps (Fig. 6c and d) were observed

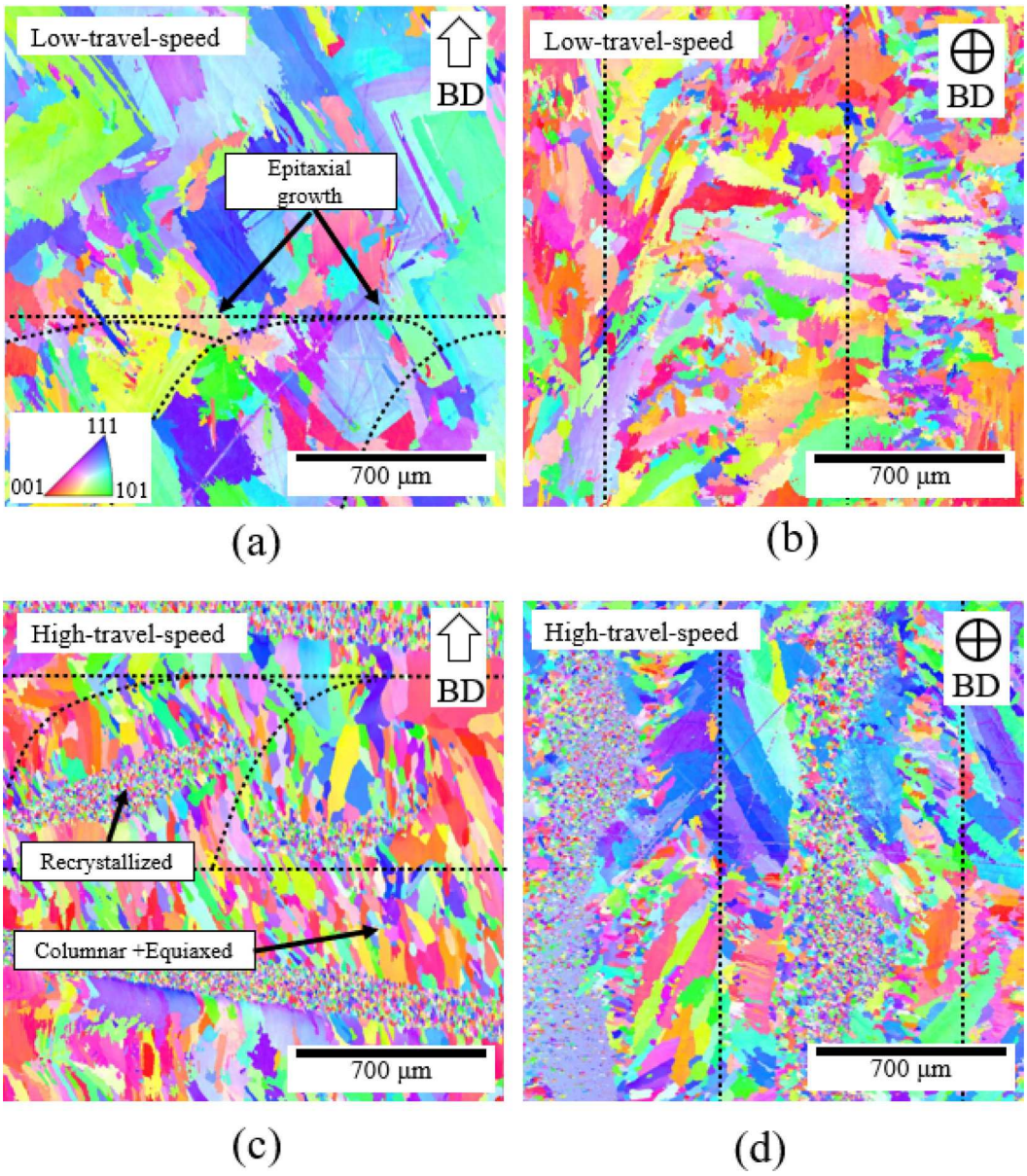


**Fig. 6.** Low-magnification EBSD crystal orientation map of (a, b) low-travel-speed sample, and (c, d) high-travel-speed sample. Dashed lines specify bead outlines.

in the same location as the non-dendritic region in the optical micrographs (Fig. 5b). Similar ultra-fine grains towards the middle of the bead have been previously observed by Bambach et al. [8] in hot wire-LDED of Inconel 718, and were attributed to incomplete melting of the wire along with recrystallization. Due to the cold work wire drawing process, the wire has high residual stress in its unmelted state. This is confirmed by EBSD micrographs of drawn wire reported by Bambach et al. [8], which show highly deformed grains. Because the high-travel-speed parameter has a relatively low energy density, and the lasers are positioned around the axially fed wire, the middle of the wire does not completely melt. However, because of the high temperature, recrystallization occurs with residual stress acting as the driving force. Zouari et al. [33] has shown that recrystallization of Inconel can occur in as little as a few seconds. This indicates that the wire could undergo recrystallization both upon deposition and from the heat of the subsequent layer deposition.

Higher magnification EBSD micrographs were collected and KAM maps were generated for low-travel-speed, and high-travel-speed samples as shown in Fig. 7a-d. In the low-travel-speed samples (Fig. 7a, b), high KAM regions are found to be relatively homogeneously distributed at sub-grain boundaries. A greater amount of high KAM regions were observed in the low-travel-speed sample when viewed perpendicular to the BD (Fig. 7b) as compared with parallel to the BD (Fig. 7a). This aligns with the crystal orientation map in Fig. 6a, which shows that the low-travel-speed grains are elongated along the BD, resulting in fewer sub-grain boundaries in the plane parallel to the BD. In the high-travel-speed samples, high KAM values were found under the recrystallized region when viewed parallel to the BD (Fig. 7c) and adjacent to the recrystallized region when viewed perpendicular to the BD (Fig. 7d). This phenomenon can be attributed to the middle of the wire not fully melting in the recrystallized region as discussed previously. The present liquid Inconel 625 solidifies around the recrystallized region; this results in a high KAM around the recrystallized region because the relatively smaller recrystallized grains create a large surface area of grain boundaries with the newly nucleated grains. However, the heat from the subsequently deposited layer allows for greater atom mobility at the top of each bead, allowing for dislocation density to decrease thereby decreasing KAM above the recrystallized region.

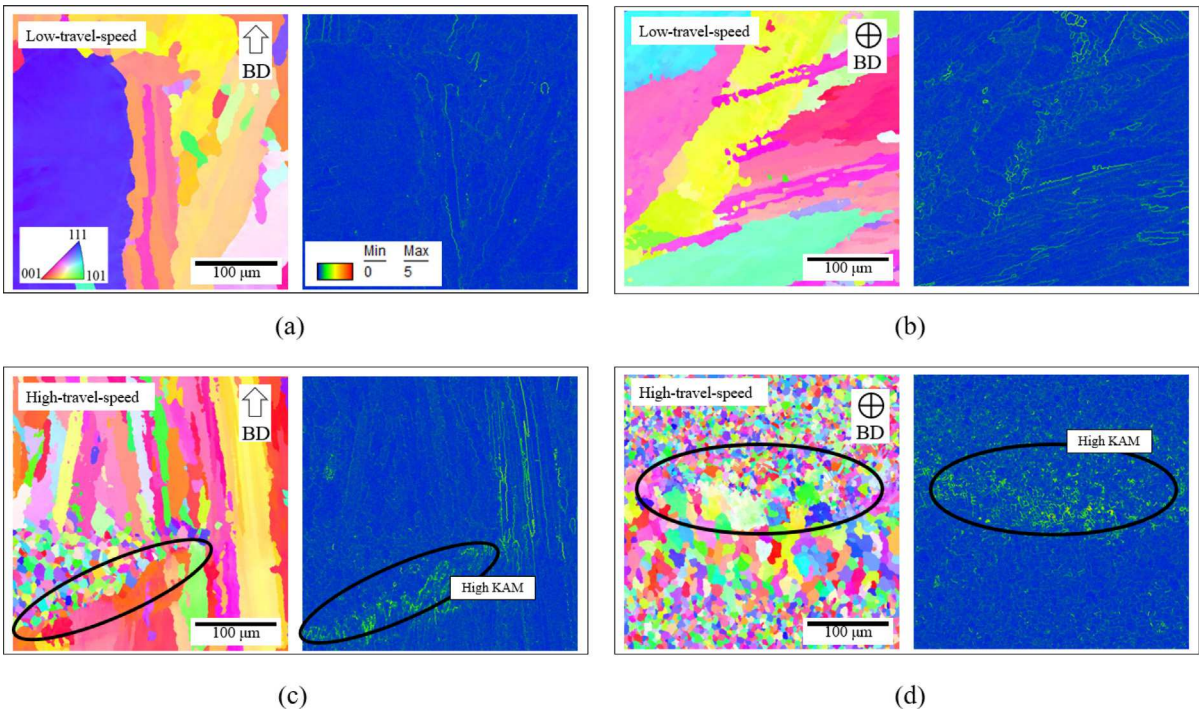


**Fig. 7.** High-magnification EBSD crystal orientation map with corresponding KAM map for (a) low-travel-speed sample parallel to the build direction, (b) low-travel-speed sample perpendicular to the build direction, (c) high-travel-speed sample parallel to the build direction, and (d) high-travel-speed sample perpendicular to the build direction. High KAM regions in the high-travel-speed samples (c and d) are circled.

### 3.3. Solidification rate and thermal gradient

The difference in grain morphology between the low-travel-speed sample (columnar grains) and high-travel-speed sample (columnar+equiaxed grains) can be explained by considering the thermal gradient $G$ and solidification rate $R$ at the solidification front. A higher $G/R$ ratio is characterized by a columnar dendritic morphology, while a lower $G/R$ ratio is characterized by an equiaxed morphology [34]. Specific $(G, R)$ values which lie at the boundary between a columnar and equiaxed microstructure are referred to as columnar-to-equiaxed transition points, and are visualized on alloy specific microstructure selection maps. To understand how processing parameters of the wire-LDED Inconel 625 fabricated in this study effect the resultant morphology, the thermal gradient $G$ and solidification rate $R$ were calculated for low-travel-speed and high-travel-speed parameters. The method outlined in Section 2.3 was used.

As detailed in Section 2.3, for calculation of solidification rate $R$, melt pool depth $D$, and melt pool length $L$ are required. A wire-LDED coupled thermo-fluid model was used to find the melt pool depth $D$ and melt pool length $L$ for the high-travel-speed and low-travel-speed parameters. The melt pool temperature distribution for the two parameters as predicted by the simulation results is shown in Fig. 8. The calculated solidification rate $R$ values along with the melt pool depth $D$ and melt pool length $L$ from the simulation are shown in Table 5. It can be seen that a higher solidification rate $R$ is calculated for high-travel-speed parameter (V = 1000 mm/min) as compared with low-travel-speed parameter (V = 400 mm/min).

To calculate $G$, the cooling rate $C_l$ was required as discussed in Section 2.3. In this study, experimentally measured $C_l$ values were used for the low-travel-speed and high-travel-speed parameters. The calculated $G$ values along with referenced $C_l$ are provided in Table 5. It is shown that the high-travel-speed parameter (power = 700 W) has a lower thermal gradient $G$ than the low-travel-speed parameter (power = 500 W). This aligns with the general trend that higher laser powers have an inverse correlation with thermal gradient, as reported by Kou [13]. By considering the solidification rate $R$ and thermal gradient $G$, a correlation with observed morphology can be made.

**Table 5**
Wire-LDED Inconel 625 melt pool dimensions and melt pool thermal parameters ($D$, $L$ are based on modeling, $C_l$ was measured experimentally, $R$ and $G$ were calculated).

| Parameter | Low-travel-speed | High-travel-speed |
|---|---|---|
| Melt pool depth ($D$) [mm] | .87 | .80 |
| Melt pool length ($L$) [mm] | 2.81 | 2.17 |
| Cooling rate ($C_l$) [K/s] | 723 | 1249 |
| Solidification rate ($R$) [m/s] | $2.1 \times 10^{-3}$ | $6.2 \times 10^{-3}$ |
| Thermal gradient ($G$) [K/m] | $3.5 \times 10^{5}$ | $2.0 \times 10^{5}$ |

Fig. 9 shows the $(G, R)$ coordinates for wire-LDED low-travel-speed and high-travel-speed parameters superimposed onto an Inconel 625 microstructure selection map developed by Hu et al. [35]. The low-travel-speed parameter lays within the columnar microstructure region. For the high-travel-speed parameter, the increase in $R$ and decrease in $G$ push the coordinate to the mixed columnar+equiaxed region. These results align with the experimental results shown in Figs. 5a-b and 6a-d, which show a columnar microstructure for low-travel-speed parameter and a columnar+equiaxed mixed microstructure for high-travel-speed parameter, respectively.

### 3.4. Mechanical properties: Stress-strain relationship

To investigate the influence of processing parameters and build orientation on mechanical properties, micro-tensile samples were fabricated using the low-travel-speed and high-travel-speed parameters and cut both perpendicular and parallel to the BD as detailed in Section 2.4. A summary of the resultant tensile properties is provided in Table 6. Representative stress–strain curves are shown in Fig. 10. In general, the measured wire-LDED yield strength and UTS for all samples lie below those reported for Inconel 625 processed via powder-LDED [36] and LPBF [37] and above the values reported for Inconel 625 processed via

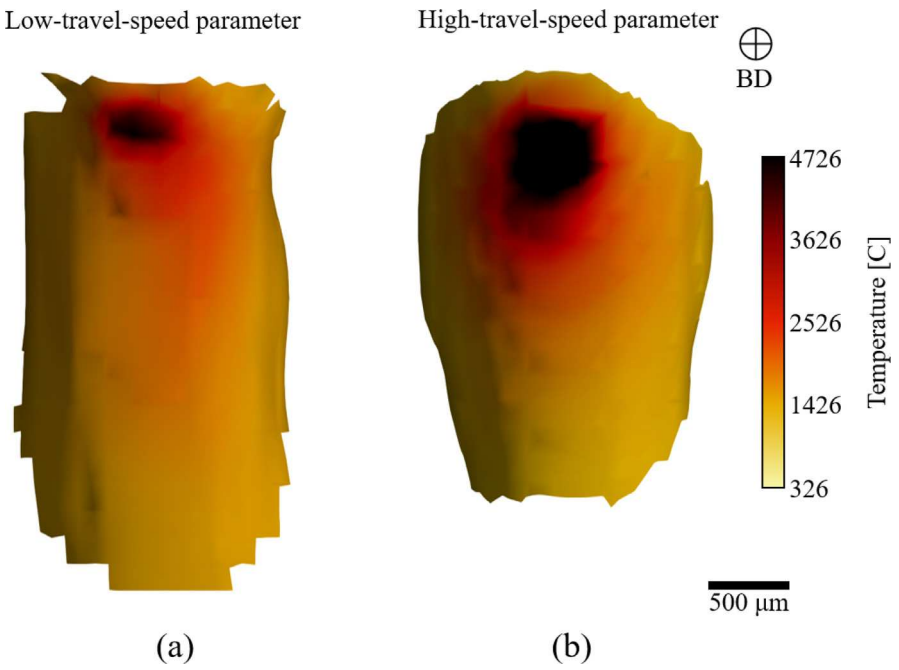


**Fig. 8.** Temperature distribution of melt pool for (a) low-travel-speed and (b) high-travel-speed based on numerical modeling. The bead edges correspond to the solidus temperature (1305 °C).

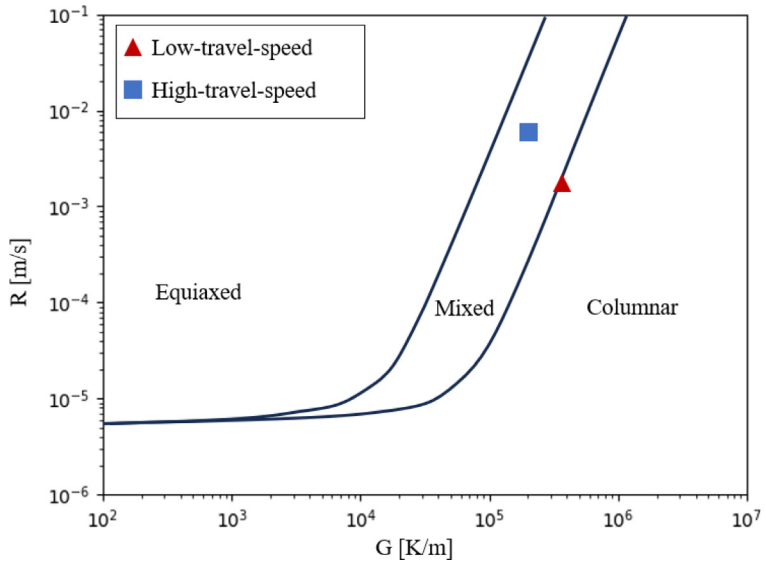


**Fig. 9.** Calculated ($G$, $R$) coordinates for low-travel-speed and high-travel-speed samples superimposed onto the Inconel 625 microstructure selection map developed by Hu et al. [35].

WAAM [38]. No significant difference was observed between tensile properties of samples fabricated using low-travel-speed versus high-travel-speed parameters when tested perpendicular to the BD. However, samples oriented parallel to the BD exhibited on average a 12% higher yield strength when fabricated using the high-travel-speed parameter compared with the low-travel-speed parameter. For both the low-travel-speed and high-travel-speed parameters, a higher yield strength is observed for the samples tested perpendicular to the BD as compared with parallel to the BD.

The principle strain evolution maps for representative low-travel-speed and high-travel-speed samples tested parallel to the BD are shown in Fig. 11. The strain distribution visualized using DIC shows no significant difference based on the orientation and parameter used to fabricate the sample. Therefore, the recrystallized grain regions in the high-travel-speed samples do not impact the strain distribution. As shown in Fig. 11, both the low-travel-speed and high-travel-speed samples show the development of multiple shear bands that stabilize until one dominates. Shear bands are commonly observed in ductile alloys, as reported by Hatherly and Malin [40]. Similar stress distributions and shear bands have been observed in powder-LDED Inconel 625 by Hu et al. [35] and Ferreira et al. [41]. After the UTS is reached, samples exhibit necking resulting in a rapid strain concentration at the point of fracture.

### 3.5. Grain boundary strengthening and dislocation strengthening

The strength of an alloy can be modeled by considering solid solution, precipitation, grain boundary, and dislocation strengthening (among other strengthening mechanisms). Both low-travel-speed and

**Table 6**
Summary of tensile properties of AM Inconel 625. The uncertainty corresponds to three standard deviations about the mean.

| Process | Orientation | Parameter | UTS MPa | 0.2% yield strength MPa | Elongation % | Source |
|---|---|---|---|---|---|---|
| Wire-LDED | Perpendicular | Low-travel-speed | 867 ± 9 | 526 ± 43 | 45 ± 11 | This study |
| Wire-LDED | Perpendicular | High-travel-speed | 870 ± 29 | 527 ± 33 | 49 ± 17 | This study |
| Wire-LDED | Parallel | Low-travel-speed | 744 ± 13 | 392 ± 14 | 56 ± 9 | This study |
| Wire-LDED | Parallel | High-travel-speed | 796 ± 15 | 437 ± 12 | 47 ± 18 | This study |
| WAAM | Parallel | – | 658 ± 4 | 373 ± 5 | 56 ± 4 | [38] |
| Wire-LDED | Perpendicular | | 785 ± 36 | 447 ± 28 | 41.5 ± 7 | [12] |
| Powder-LDED | N/A | – | 944 ± 12 | 524 ± 13 | 35 ± 4 | [36] |
| LPBF | Parallel | – | 1121 ± 7 | 845 ± 18 | 41 ± 0.4 | [37] |
| Wrought | – | – | 914 ± 18 | 413 ± 8 | 70 ± 4 | [39] |

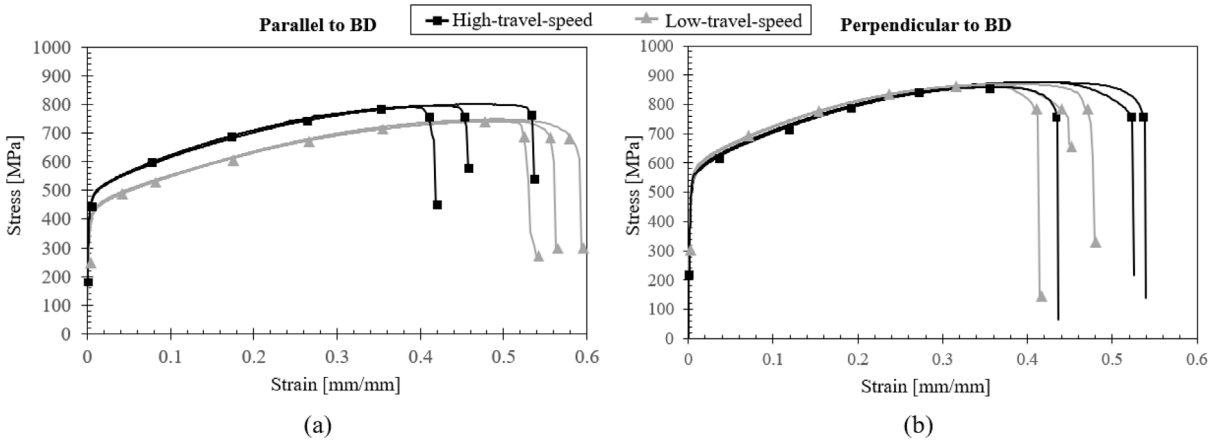


**Fig. 10.** Stress–strain curves for the high-travel-speed and low-travel-speed parameters tested (a) parallel and (b) perpendicular to the build direction (BD).

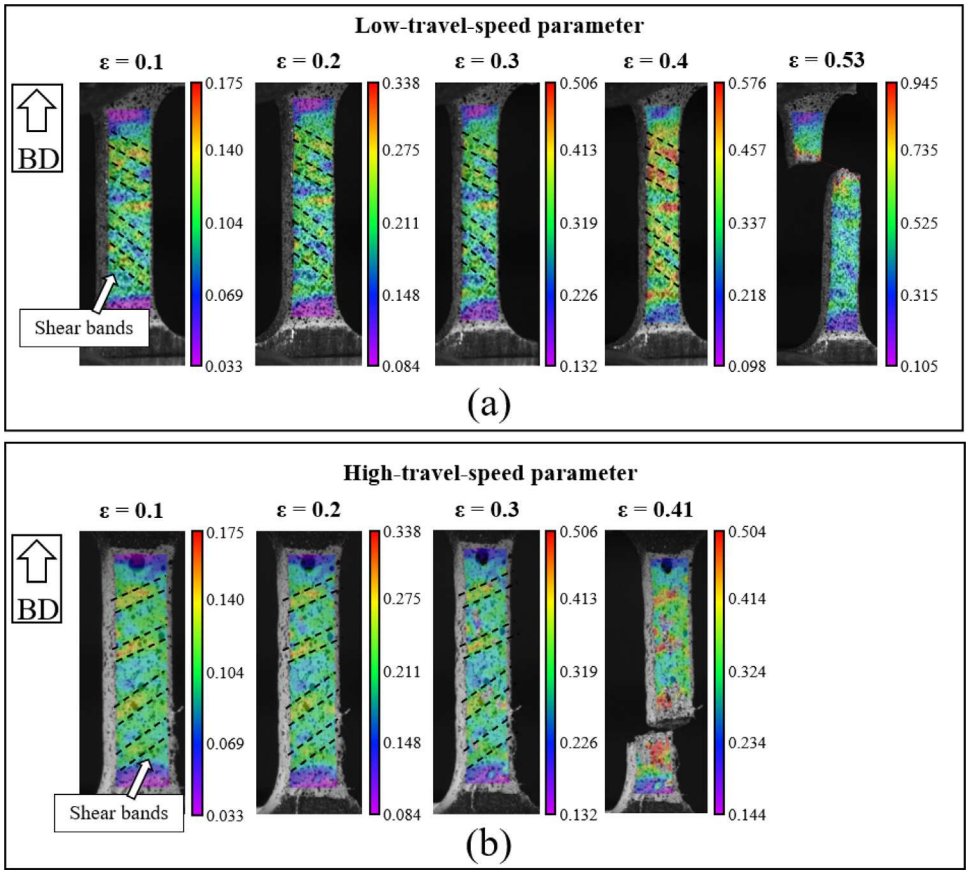


**Fig. 11.** Principle strain map evolution for a low-travel-speed sample and high-travel-speed sample tested parallel to the build direction. The arrows point towards shear bands.

**Table 7**
Calculated influence of grain boundary strengthening. All values relative to the low-travel-speed parameter, parallel yield strength.

| Orientation | Parameter | Average grain size (μm) | Hall petch ($\Delta\sigma_{GB}$) (MPa) |
|---|---|---|---|
| Parallel | Low-travel-speed | 198 | 0 |
| Perpendicular | Low-travel-speed | 81 | 30 |
| Parallel | High-travel-speed | 85[a] | 27 |
| Perpendicular | High-travel-speed | 86[a] | 28 |

[a] For the high-travel-speed parameter, the average grain size was calculated based on only the average of the columnar+equiaxed grain region (not the recrystallized grain region).

high-travel-speed samples were fabricated using the same feedstock, meaning that the solid solution strengthening effect is nearly identical for all parameters and orientations tested. In addition, XRD results in Appendix C do not suggest the presence of precipitates in wire-LDED Inconel 625, indicating the precipitation strengthening effect is not responsible for the measured differences in yield strength. Therefore, observed differences in yield strength are analyzed in terms of grain boundary and dislocation strengthening.

### 3.5.1. Grain boundary strengthening

Grain boundary strengthening occurs when dislocation movement is impeded by dissimilarly oriented lattices at grain boundaries, resulting in a higher yield strength. To calculate the grain boundary strengthening for each parameter and orientation tested, the Hall-Petch relationship (Eq. (3)) was used. As detailed in Section 2.5.1, the average grain size $d$ is required; this value was calculated from the low-magnification EBSD data shown in Fig. 6 (the grain size distribution for each micrograph is provided in Appendix B). The yield strength of recrystallized regions has been shown to be far above its non-recrystallized counterpart [42]. Such recrystallized regions were observed within the center of the bead in the high-travel-speed samples (Fig. 6c, d). Therefore, the yield strength of the high-travel-speed samples is governed by the strength of the columnar+equiaxed grain regions rather than recrystallized grain regions. For this reason, the average grain size from the columnar+equiaxed grain region was used to calculate $d$ for high-travel-speed parameter rather than the overall average grain size.

The $\Delta\sigma_{GB}$ was calculated for each condition relative to the low-travel-speed, parallel orientation. The results, shown in Table 7, indicate the smaller columnar+equiaxed grain size in the high-travel-speed parallel orientation results in a 27 MPa increase in yield strength relative to the low-travel-speed parallel orientation columnar grains. This value is substantially higher than the 8.6 MPa difference in Hall-Petch strengthening between an equiaxed and columnar grain microstructure reported by Li et al. [15] for WAAM Inconel 625, indicating that low-travel-speed adjustments in wire-LDED can lead to more significant grain size refinement than WAAM. Hall-Petch strengthening results in a 30 MPa increase in yield strength for the low-travel-speed perpendicular orientation relative to its parallel counterpart, pointing towards the anisotropy of the low-travel-speed grain morphology. Hall-Petch has been previously shown to be responsible for differences in strength relative to the build direction in high entropy [43] and 316L samples [44] fabricated using LPBF. The strength increase for the high-travel-speed parallel and perpendicular orientations was relatively similar (27 and 28 MPa, respectively), indicating a relatively isotropic grain morphology.

### 3.5.2. Dislocation strengthening

When a large number of dislocations are present in a material, the dislocations tend to impede motion due to difficulty of dislocation glide through lattice imperfections [45]. This results in dislocation strengthening. Dislocations can be introduced into a material both through rapid solidification and thermal stress [46,47]. To calculate dislocation strengthening for each parameter and orientation tested, the method outlined in Section 2.5.2 was used. As discussed in Section 2.5.2, for calculation of dislocation strengthening the Taylor factor $M$ and dislocation density $\rho$ are required. The Taylor factor was calculated based on the low-magnification EBSD micrographs shown in Fig. 6a-d, and was found to be relatively similar for all parameters and orientations as shown in Table 8.

**Table 8**
Average Taylor factor and dislocation density as a function of low-travel-speed and orientation.

| Orientation | Parameter | Taylor factor | Dislocation density $m^{-2}$ |
|---|---|---|---|
| Parallel | Low-travel-speed | 2.86 | $4.13 \times 10^{14}$ |
| Perpendicular | Low-travel-speed | 2.97 | $9.91 \times 10^{14}$ |
| Parallel | High-travel-speed | 2.86 | $5.99 \times 10^{14}$ |
| Perpendicular | High-travel-speed | 3.09 | $6.95 \times 10^{14}$ |

**Table 9**
Calculated influence of dislocation strengthening. All values relative to the low-travel-speed parameter, parallel yield strength. All values relative to the low-travel-speed, parallel yield strength.

| Orientation | Parameter | Dislocation strengthening ($\Delta\sigma_D$) MPa |
|---|---|---|
| Parallel | Low-travel-speed | 0 |
| Perpendicular | Low-travel-speed | 105 |
| Parallel | High-travel-speed | 52 |
| Perpendicular | High-travel-speed | 70 |

Dislocation density was calculated using the method discussed in Section 2.5.2 by using average KAM values from the high-magnification EBSD data in Fig. 7a-d. For the high-travel-speed samples, the average KAM values used in Eq. (5) were calculated from the columnar+equiaxed grain region sufficient distance away from the recrystallized region where a lower average KAM was observed (Fig. 7c, d). This is because (per Eqs. (4) and (5)) a higher KAM region will have increased strength. Because overall strength of a material is governed by strength of the weakest region, using the lower KAM region is representative of the overall strength. The results of the dislocation density calculation are provided in Table 8, and show that significantly different dislocation densities are observed between all parameters and orientations.

$\Delta\sigma_D$ was calculated for each condition relative to the low-travel-speed, parallel orientation. The results, shown in Table 9, suggest that dislocation strengthening contributes significantly to the difference in strength observed between the high-travel-speed, parallel yield strength and the low-travel-speed, parallel yield strength. Table 9 also shows that dislocation strengthening, driven by a difference in dislocation density (Table 8), is largely responsible for the increase in strength observed between the low-travel-speed parallel and perpendicular orientation. This result aligns with results published by Mukherjee [48], where a higher average KAM was measured on the plane perpendicular to the BD as compared with parallel to the BD in powder-LDED printed 316L stainless steel. Due to a similar dislocation density and Taylor factor, a relatively small difference (18 MPa) in dislocation strengthening was observed between the high-travel-speed parallel and perpendicular samples.

The total calculated difference in strength $\Delta\sigma_T$ using Eq. (6) is given in Table 10. The calculated increase in strength between the low-travel-speed perpendicular and parallel orientations is remarkably close the experimental value (135 MPa calculated, 134 MPa experimental). The calculated increase in strength for the high-travel-speed parallel yield strength is significantly higher than the experimental result. Conversely, the increase in strength for the high-travel-speed perpendicular

**Table 10**
Calculated influence of grain boundary and dislocation strengthening on experimental differences in values of yield strength. All values relative to the low-travel-speed, parallel yield strength.

| Orientation | Parameter | Total calculated ($\sigma_T$) MPa | Experimental results MPa |
|---|---|---|---|
| Parallel | Low-travel-speed | 0 | 0 |
| Perpendicular | Low-travel-speed | 135 | 134 |
| Parallel | High-travel-speed | 79 | 45 |
| Perpendicular | High-travel-speed | 98 | 135 |

yield strength is significantly lower than the experimental result. The discrepancy between the calculated and experimental values for the high-travel-speed parameter can be explained by the fact that the relevant factors for dislocation and grain boundary strengthening (KAM, Taylor factor, grain size) were approximated based on a 2D cross section. For low-travel-speed samples, this is a valid approximation since the in-plane microstructure is shown to be relatively constant relative to the plane scanned (Fig. 6a, b). On the other hand, the bimodal grain size distribution of high-travel-speed samples results in a significantly different microstructure depending on the cross-section scanned (Fig. 6c, d), resulting in the observed erroneous calculated yield strength. More accurate modeling of the strengthening in highly complex bi-modal microstructures such as the one observed in the high-travel-speed samples serves as motivation for the development of three-dimensional characterization techniques.

$$\Delta\sigma_T = \Delta\sigma_{GB} + \Delta\sigma_D \tag{6}$$

## 4. Conclusion

In this work, an array of parameters was tested to establish a processing map for wire-LDED of Inconel 625. Based on this processing map, a low-travel-speed parameter (Parameter A, 500 W 400 mm/min) and a high-travel-speed parameter (Parameter F, 700 W 1000 mm/min) which showed no defects were selected for further characterization in terms of grain morphology and mechanical properties. Based on the results of this characterization, the following conclusions can be drawn:

- The low-travel-speed parameter results in a columnar grains elongated in the BD. The high-travel-speed sample shows refined columnar+equiaxed grains towards the top and bottom of each bead. A recrystallized region is observed in the middle of the bead of the high-travel-speed sample, and is attributed to incomplete wire remelting.
- The low-travel-speed parameter is shown to result in a lower solidification rate $R$ and higher thermal gradient $G$ than the high-travel-speed parameter. By coupling the calculated $R$ and $G$ for each parameter with a existing solidification map of Inconel 625, it is shown that the low-travel-speed parameter exists within the columnar region, while the high-travel-speed parameter exists in the mixed columnar+equiaxed region, thus providing a mechanism for the experimentally observed microstructure.
- When tested parallel to the BD, a higher yield strength is observed in the high-travel-speed parameter than the low-travel-speed parameter. When tested perpendicular to the BD, a similar yield strength is observed between the two parameters. For both parameters, the tensile samples tested perpendicular the BD exhibit a higher yield strength than the samples tested parallel to the BD.
- A comparative analysis of the strengthening mechanisms of the wire-LDED printed samples was conducted, and indicates that dislocation strengthening is primarily responsible for the observed differences in yield strength between the parameters and orientations tested. The differences in dislocation strengthening are driven by differences in dislocation density.

## CRediT authorship contribution statement

**Jakub Preis:** Writing – original draft, Methodology, Investigation, Formal analysis, Conceptualization. **Stephanie B. Lawson:** Writing – review & editing, Software, Investigation. **Isshu Lee:** Writing – review & editing, Investigation. **Megumi Kawasaki:** Writing – review & editing, Resources. **Brian K. Bay:** Writing – review & editing, Resources. **Sriram Manoharan:** Methodology. **Brian K. Paul:** Writing – review & editing, Resources, Project administration, Funding acquisition. **Somayeh Pasebani:** Writing – review & editing, Supervision, Resources, Project administration, Funding acquisition.

## Declaration of competing interest

The authors declare that they have no known competing financial interests or personal relationships that could have appeared to influence the work reported in this paper.

## Data availability

The raw/processed data required to reproduce these findings cannot be shared at this time as the data also forms part of an ongoing study.

## Acknowledgments

This work relates to Department of Navy award (Award Number N00014-20-1-2836 in collaboration with University of Tennessee, Knoxville) issued by the Office of Naval Research. The United States Government has a royalty-free license throughout the world in all copyrightable material contained herein. Any opinions, findings, and conclusions or recommendations expressed in this material are those of the author(s) and do not necessarily reflect the views of the Office of Naval Research. Additionally, SP and KP greatly acknowledge the funding from the National Science Foundation, United States (NSF CAREER award # 2338253). SP and JP would like to sincerely acknowledge Dr. Nick Wannenmacher, Mr. Mark Rice and Mrs. Maria Wright for their technical support and project management. The authors thank Peter Eschbach at the OSU electron microscopy center.

## Appendix A. Comparing micro-tensile geometry to ASTM E8 geometry

In this study, a micro-tensile geometry was utilized combined with a relatively high strain rate providing the following advantages: (1) a shorter fabrication time and (2) less time per test. To allow for a greater confidence in the measured mechanical properties in this study, a preliminary investigation was conducted comparing the mechanical properties of the subsize ASTM E8 specimen tested at a lower strain rate and the utilized micro-tensile geometry. For the comparison, E8 subsize specimens of dimensions provided in Fig. A.1 were cut at an orientation perpendicular to the BD from a block printed using the low-travel-speed parameter. Three tensile specimens with the configuration of ASTM E8 specimens were tested using an Instron 5982 with a strain rate of $10^{-4}$ $s^{-1}$.

The results of the study are provided in Table A.1. No significant difference is observed in the mechanical properties of the two samples. The UTS, yield strength, and elongation of the micro-tensile geometry all lie within the three standard deviations of the mean of the ASTM E8 tensile properties. Future studies will use the same load frame, grips, and strain rate to isolate the size effect of the micro-tensile geometry.

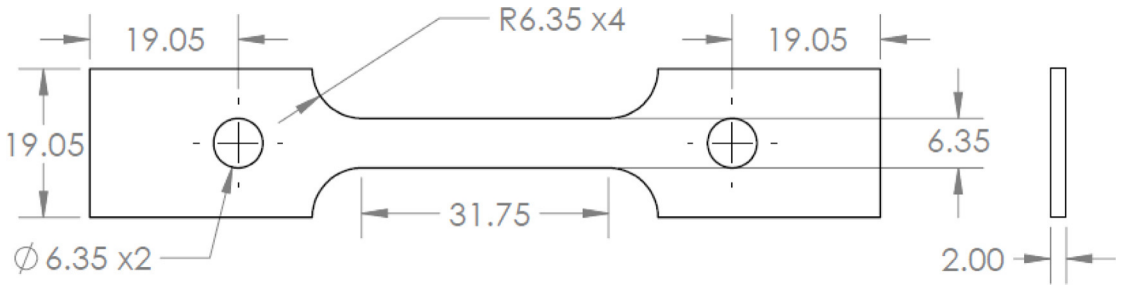


**Fig. A.1.** Dimensions of ASTM E8 subsize specimen [49].

**Table A.1**
Comparison of mechanical properties derived from the ASTM E8 tensile geometry and micro-tensile geometry used for this study.

| Geometry | Direction | Parameter | UTS MPa | 0.2% yield strength MPa | Elongation % |
|---|---|---|---|---|---|
| ASTM E8 | Perpendicular | Low-travel-speed | 805 ± 65 | 541 ± 65 | 47 ± 7 |
| Micro-tensile | Perpendicular | Low-travel-speed | 867 ± 9 | 526 ± 43 | 45 ± 11 |

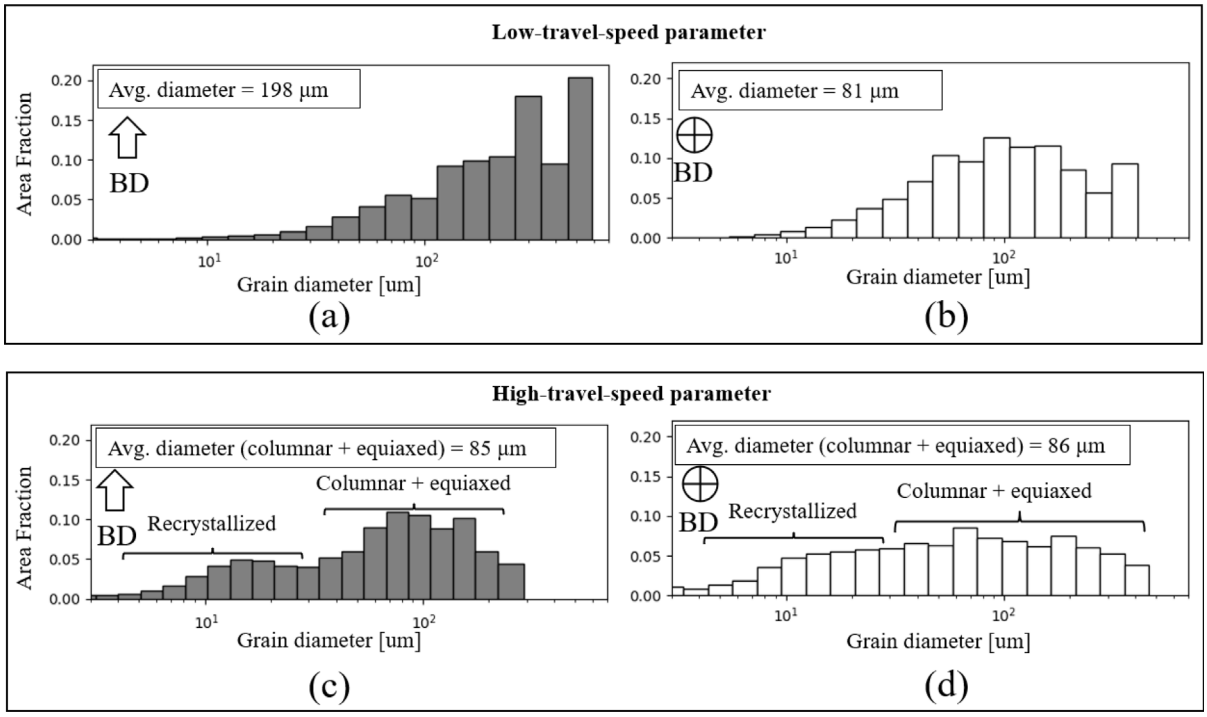


**Fig. B.1.** Grain size distribution for (a) low-travel-speed sample parallel to the build direction, (b) low-travel-speed sample perpendicular to the build direction, (c) high-travel-speed sample parallel to the build direction, and (d) high-travel-speed sample perpendicular to the build direction. For the high-travel-speed parameter only the columnar+equiaxed average grain size is provided because these are the values used in the analysis outlined in Section 3.5.1.

## Appendix B. Grain size distribution

See Fig. B.1.

## Appendix C. XRD results

XRD was performed using a Rigaku Smartlab XRD with a Cu source to detect present phases. An aperture width of 5 × 2 mm was used to select the exposure region. A generator voltage of 40 kV and current of 44 mA was used. The $2\theta$ from 20° to 80° was measured with an increment of 0.02° and a time step of 4 s. Previous studies on power LDED have shown a presence of carbides with volume fractions high enough to be detected by XRD [32,36]. Carbides are known to decrease elongation with no increase in yield strength because they deplete Cr and Mo at the grain boundaries, and are therefore undesirable [50,51]. The presence of carbides depends on whether the deposited material is heated to a sufficiently high temperature (between 750 °C and 980 °C [52]) for enough time to allow for precipitation to take place. The wire-LDED XRD results in Fig. C.1 show that only peaks corresponding to the $\gamma$ FCC phase and no peaks corresponding to carbides were observed in both the low-travel-speed parameter (low-travel-speed) and high-travel-speed parameter (high-travel-speed).

Jackman et al. [50] reported that a carbon content of .008 wt% in Inconel shows no evidence of carbides and has a higher toughness relative to Inconel with higher carbon levels. The relatively low carbon content of the Inconel wire used for this study (.01 wt% C, Table 1) provides further evidence that carbides should not play a role in effecting the mechanical properties of the printed wire-LDED samples.

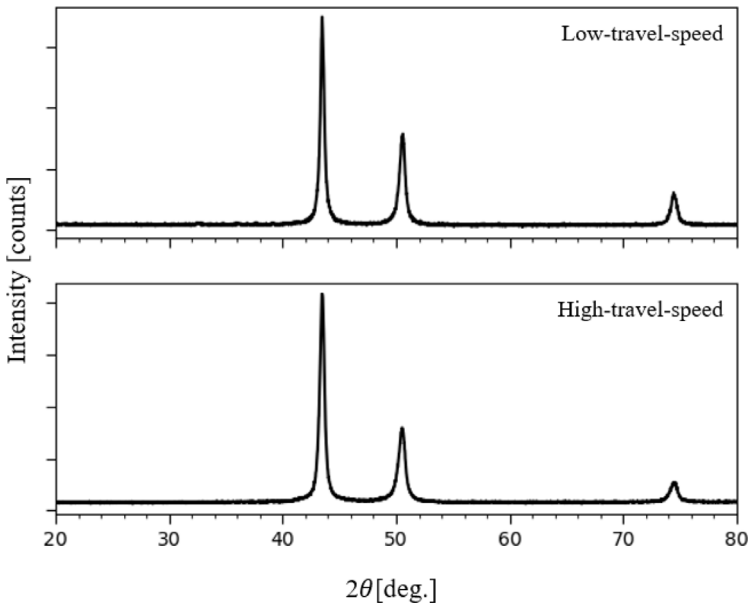


**Fig. C.1.** XRD scans of the low-travel-speed and high-travel-speed samples showing only $\gamma$ FCC peaks.

It should be taken into account that XRD has been shown to not detect phases which occupy a volume fraction less than 0.02 [53].

## References


[1] N. Ghanadi, S. Pasebani, A review on wire-laser directed energy deposition: Parameter control, process stability, and future research paths, J. Manuf. Mater. Process. 8 (2) (2024) http://dx.doi.org/10.3390/jmmp8020084, URL https://www.mdpi.com/2504-4494/8/2/84.

[2] J. Preis, Z. Wang, J. Howard, Y. Lu, N. Wannenmacher, S. Shen, B.K. Paul, S. Pasebani, Effect of laser power and deposition sequence on microstructure of GRCop42 - Inconel 625 joints fabricated using laser directed energy deposition, Mater. Des. 241 (2024a) 112944, http://dx.doi.org/10.1016/J.MATDES.2024.112944, URL https://linkinghub.elsevier.com/retrieve/pii/S0264127524003186.

[3] J. Preis, D. Xu, B.K. Paul, P.A. Eschbach, S. Pasebani, Effect of liquid miscibility gap on defects in inconel 625–GRCop42 joints through analysis of gradient composition microstructure, J. Manuf. Mater. Process. 8 (1) (2024b) http://dx.doi.org/10.3390/jmmp8010042, URL https://www.mdpi.com/2504-4494/8/1/42.

[4] L.D. Harwell, M.L. Griffith, D.L. Greene, G.A. Pressly, Energetic additive manufacturing process with feed wire, Patentschrift (US006143378A) (1999).

[5] W.U.H. Syed, A.J. Pinkerton, L. Li, A comparative study of wire feeding and powder feeding in direct diode laser deposition for rapid prototyping, Appl. Surf. Sci. 247 (1–4) (2005) http://dx.doi.org/10.1016/j.apsusc.2005.01.138.

[6] S. Nowotny, F. Brueckner, S. Thieme, C. Leyens, E. Beyer, High-performance laser cladding with combined energy sources, J. Laser Appl. 27 (S1) (2015) http://dx.doi.org/10.2351/1.4817455.

[7] J. Kelbassa, A. Gasser, J. Bremer, O. Pütsch, R. Poprawe, J. Henrich Schleifenbaum, Equipment and process windows for laser metal deposition with coaxial wire feeding, J. Laser Appl. 31 (2) (2019) http://dx.doi.org/10.2351/1.5096112.

[8] M. Bambach, I. Sizova, F. Kies, C. Haase, Directed energy deposition of Inconel 718 powder, cold and hot wire using a six-beam direct diode laser set-up, Addit. Manuf. 47 (2021) http://dx.doi.org/10.1016/j.addma.2021.102269.

[9] S. Zhou, T. Xu, C. Hu, H. Wu, H. Liu, X. Ma, Effect of different topologies on microstructure and mechanical properties of multilayer coatings deposited by laser cladding with inconel 625 wire, Surf. Coat. Technol. 421 (2021) 127299, http://dx.doi.org/10.1016/J.SURFCOAT.2021.127299.

[10] T.E. Abioye, P.K. Farayibi, A.T. Clare, A comparative study of Inconel 625 laser cladding by wire and powder feedstock, Mater. Manuf. Process. 32 (14) (2017) http://dx.doi.org/10.1080/10426914.2017.1317787.

[11] A. Gamon, E. Arrieta, P.R. Gradl, C. Katsarelis, L.E. Murr, R.B. Wicker, F. Medina, Microstructure and hardness comparison of as-built inconel 625 alloy following various additive manufacturing processes, Res. Mater. 12 (2021) http://dx.doi.org/10.1016/j.rinma.2021.100239.

[12] G. Su, Y. Shi, G. Li, G. Zhang, Y. Xu, Improving the deposition efficiency and mechanical properties of additive manufactured Inconel 625 through hot wire laser metal deposition, J. Mater. Process. Technol. 322 (2023) 118175, http://dx.doi.org/10.1016/J.JMATPROTEC.2023.118175.

[13] S. Kou, Welding metallurgy, 2002, http://dx.doi.org/10.1002/0471434027.

[14] N. Raghavan, R. Dehoff, S. Pannala, S. Simunovic, M. Kirka, J. Turner, N. Carlson, S.S. Babu, Numerical modeling of heat-transfer and the influence of process parameters on tailoring the grain morphology of IN718 in electron beam additive manufacturing, Acta Mater. 112 (2016) 303–314, http://dx.doi.org/10.1016/J.ACTAMAT.2016.03.063.

[15] S. Li, J.Y. Li, Z.W. Jiang, Y. Cheng, Y.Z. Li, S. Tang, J.Z. Leng, H.X. Chen, Y. Zou, Y.H. Zhao, J.P. Oliveira, Y. Zhang, K.H. Wang, Controlling the columnar-to-equiaxed transition during Directed Energy Deposition of Inconel 625, Addit. Manuf. 57 (2022) 102958, http://dx.doi.org/10.1016/J.ADDMA.2022.102958.

[16] M. Akbari, Y. Ding, R. Kovacevic, Process development for a robotized laser wire additive manufacturing, in: ASME 2017 12th International Manufacturing Science and Engineering Conference, MSEC 2017 Collocated with the JSME/ASME 2017 6th International Conference on Materials and Processing, Vol. 2, 2017, http://dx.doi.org/10.1115/MSEC2017-2951.

[17] ASTM, ASTM B311-17: Standard Test Method for Density of Powder Metallurgy ( PM ) Materials Containing Less Than Two Percent Porosity, ASTM International, 2019.

[18] G.L. Wynick, C.J. Boehlert, Use of electropolishing for enhanced metallic specimen preparation for electron backscatter diffraction analysis, Mater. Charact. 55 (3) (2005) 190–202, http://dx.doi.org/10.1016/J.MATCHAR.2005.04.008.

[19] Y. Li, A. Olmedilla, M. Založnik, J. Zollinger, L. Dembinski, A. Mathieu, Solidification microstructure during selective laser melting of Ni based superalloy: Experiment and mesoscopic modelling, in: IOP Conference Series: Materials Science and Engineering, Vol. 529, 2019, http://dx.doi.org/10.1088/1757-899X/529/1/012004.

[20] S. Lawson, M. Ghayoor, A. Tabei, S. Pasebani, Thermal profile modeling and microstructural evolution in laser processing of inconel 625 plates, 2023, PREPRINT (Version 1) available at Research Square.

[21] Small specimen test techniques: 6th volume, 2015, http://dx.doi.org/10.1520/stp1576-eb.

[22] I. Jones, R. Bigger, B. Blaysat, C. Boo, M. Grewer, J. Hu, A. Jones, M. Klein, K. Raghavan, P. Reu, T. Schmidt, T. Siebert, M. Simenson, D. Turner, A. Vieira, T. Weikert, A good practices guide for digital image correlation, in: International Digital Image Correlation Society, 2018.

[23] N. Hansen, Hall–Petch relation and boundary strengthening, Scr. Mater. 51 (8) (2004) 801–806, http://dx.doi.org/10.1016/J.SCRIPTAMAT.2004.06.002.

[24] R.W. Kozar, A. Suzuki, W.W. Milligan, J.J. Schirra, M.F. Savage, T.M. Pollock, Strengthening mechanisms in polycrystalline multimodal nickel-base superalloys, Metall. Mater. Trans. A 40 (7) (2009) http://dx.doi.org/10.1007/s11661-009-9858-5.

[25] K. Li, J. Li, B. Tang, W.Y. Wang, F. Chen, M. Zhang, J. Fan, H. Zhong, Experimental and simulation analysis of residual topography dominated deformation mechanism of nanoindentation: a case study of Inconel 625 superalloy, J. Mater. Res. Technol. 13 (2021) 1521–1533, http://dx.doi.org/10.1016/J.JMRT.2021.05.054.

[26] T.G. I, Plastic strain in metals, J. Inst. Met. 62 (1938) 307–324, URL https://cir.nii.ac.jp/crid/1571135650487126144.bib?lang=en.

[27] H. Mughrabi, The $\alpha$-factor in the Taylor flow-stress law in monotonic, cyclic and quasi-stationary deformations: Dependence on slip mode, dislocation arrangement and density, Curr. Opin. Solid State Mater. Sci. 20 (6) (2016) 411–420, http://dx.doi.org/10.1016/J.COSSMS.2016.07.001.

[28] M. Calcagnotto, D. Ponge, E. Demir, D. Raabe, Orientation gradients and geometrically necessary dislocations in ultrafine grained dual-phase steels studied by 2D and 3D EBSD, Mater. Sci. Eng. A 527 (10–11) (2010) 2738–2746, http://dx.doi.org/10.1016/J.MSEA.2010.01.004.
[29] M. Kamaya, Assessment of local deformation using EBSD: Quantification of accuracy of measurement and definition of local gradient, Ultramicroscopy 111 (8) (2011) 1189–1199, http://dx.doi.org/10.1016/J.ULTRAMIC.2011.02.004.
[30] S.C. Bozeman, O.B. Isgor, J.D. Tucker, Effects of processing conditions on the solidification and heat-affected zone of 309L stainless steel claddings on carbon steel using wire-directed energy deposition, Surf. Coat. Technol. 444 (2022) 128698, http://dx.doi.org/10.1016/J.SURFCOAT.2022.128698.
[31] ASTM International, Standard Test Method for Density of Powder Metallurgy ( PM ) Materials Containing Less Than Two Percent Porosity, Vol. i, ASTM International, 2017.
[32] M. Rombouts, G. Maes, M. Mertens, W. Hendrix, Laser metal deposition of Inconel 625: Microstructure and mechanical properties, J. Laser Appl. 24 (5) (2012) http://dx.doi.org/10.2351/1.4757717.
[33] M. Zouari, R.E. Logé, N. Bozzolo, In situ characterization of inconel 718 post-dynamic recrystallization within a scanning electron microscope, Metals 7 (11) (2017) http://dx.doi.org/10.3390/met7110476.
[34] W. Kurz, C. Bezençon, M. Gäumann, Columnar to equiaxed transition in solidification processing, Sci. Technol. Adv. Mater. 2 (1) (2001) http://dx.doi.org/10.1016/S1468-6996(01)00047-X.
[35] Y.L. Hu, X. Lin, S.Y. Zhang, Y.M. Jiang, X.F. Lu, H.O. Yang, W.D. Huang, Effect of solution heat treatment on the microstructure and mechanical properties of Inconel 625 superalloy fabricated by laser solid forming, J. Alloys Compd. 767 (2018) 330–344, http://dx.doi.org/10.1016/J.JALLCOM.2018.07.087.
[36] J. Dutkiewicz, L. Rogal, D. Kalita, K. Berent, B. Antoszewski, H. Danielewski, M. St. Weglowski, M. Lazinska, T. Durejko, T. Czujko, Microstructure and properties of inconel 625 fabricated using two types of laser metal deposition methods, Materials 13 (21) (2020) http://dx.doi.org/10.3390/ma13215050.
[37] M.A. Anam, Microstructure and Mechanical Properties of Selective Laser Melted Superalloy Inconel 625, Elsevier, 2018.
[38] A.N. Tanvir, M.R. Ahsan, G. Seo, J.d. Kim, C. Ji, B. Bates, Y. Lee, D.B. Kim, Heat treatment effects on Inconel 625 components fabricated by wire + arc additively manufacturing (WAAM)—part 2: mechanical properties, Int. J. Adv. Manuf. Technol. 110 (7–8) (2020) http://dx.doi.org/10.1007/s00170-020-05980-w.
[39] K.S. Kim, T.H. Kang, M.E. Kassner, K.T. Son, K.A. Lee, High-temperature tensile and high cycle fatigue properties of inconel 625 alloy manufactured by laser powder bed fusion, Addit. Manuf. 35 (2020) http://dx.doi.org/10.1016/j.addma.2020.101377.
[40] M. Hatherly, A.S. Malin, Shear bands in deformed metals, Scr. Metall. 18 (5) (1984) 449–454, http://dx.doi.org/10.1016/0036-9748(84)90419-8.
[41] A.A. Ferreira, A.R. Reis, R.L. Amaral, J.M. Cruz, P.C. Romio, J.O. Seabra, M.F. Vieira, Mechanical and microstructural characterisation of bulk Inconel 625 produced by direct laser deposition, Mater. Sci. Eng. A 838 (2022) 142777, http://dx.doi.org/10.1016/J.MSEA.2022.142777.
[42] Y. Wang, J. Shi, Recrystallization behavior and tensile properties of laser metal deposited Inconel 718 upon in-situ ultrasonic impact peening and heat treatment, Mater. Sci. Eng. A 786 (2020) 139434, http://dx.doi.org/10.1016/J.MSEA.2020.139434.
[43] J.M. Park, J. Choe, H.K. Park, S. Son, J. Jung, T.S. Kim, J.H. Yu, J.G. Kim, H.S. Kim, Synergetic strengthening of additively manufactured (CoCrFeMnNi)99C1 high-entropy alloy by heterogeneous anisotropic microstructure, Addit. Manuf. 35 (2020) 101333, http://dx.doi.org/10.1016/J.ADDMA.2020.101333.
[44] S. Bahl, S. Mishra, K.U. Yazar, I.R. Kola, K. Chatterjee, S. Suwas, Non-equilibrium microstructure, crystallographic texture and morphological texture synergistically result in unusual mechanical properties of 3D printed 316L stainless steel, Addit. Manuf. 28 (2019) 65–77, http://dx.doi.org/10.1016/J.ADDMA.2019.04.016.
[45] N. Kamikawa, X. Huang, N. Tsuji, N. Hansen, Strengthening mechanisms in nanostructured high-purity aluminium deformed to high strain and annealed, Acta Mater. 57 (14) (2009) http://dx.doi.org/10.1016/j.actamat.2009.05.017.
[46] K.M. Bertsch, G. Meric de Bellefon, B. Kuehl, D.J. Thoma, Origin of dislocation structures in an additively manufactured austenitic stainless steel 316L, Acta Mater. 199 (2020) 19–33, http://dx.doi.org/10.1016/J.ACTAMAT.2020.07.063.
[47] M. Lindroos, T. Pinomaa, K. Ammar, A. Laukkanen, N. Provatas, S. Forest, Dislocation density in cellular rapid solidification using phase field modeling and crystal plasticity, Int. J. Plast. 148 (2022) 103139, http://dx.doi.org/10.1016/J.IJPLAS.2021.103139.
[48] M. Mukherjee, Effect of build geometry and orientation on microstructure and properties of additively manufactured 316L stainless steel by laser metal deposition, Materialia 7 (2019) 100359, http://dx.doi.org/10.1016/J.MTLA.2019.100359.
[49] ASTM, ASTM E8/E8M standard test methods for tension testing of metallic materials, in: Annual Book of ASTM Standards, 2021, (C).
[50] L. Jackman, M. Boldy, A. Coffey, The influence of reduced carbon on alloy 718, 1991, http://dx.doi.org/10.7449/1991/superalloys_1991_261_270.
[51] M. Sundararaman, P. Mukhopadhyay, S. Banerjee, Carbide precipitation in nickel base superalloys 718 and 625 and their effect on mechanical properties, 2012, http://dx.doi.org/10.7449/1997/superalloys_1997_367_378.
[52] M. Karmuhilan, S. Kumanan, A review on additive manufacturing processes of inconel 625, 2022, http://dx.doi.org/10.1007/s11665-021-06427-3.
[53] H. Khan, A.S. Yerramilli, A. D'Oliveira, T.L. Alford, D.C. Boffito, G.S. Patience, Experimental methods in chemical engineering: X-ray diffraction spectroscopy—XRD, 2020, http://dx.doi.org/10.1002/cjce.23747.